

A Novel Multicompartment Barrier-Free Microfluidic Device Reveals the Impact of Extracellular Matrix Stiffening and Temozolomide on Immune-Tumor Interactions in Glioblastoma

Clara Bayona, Claudia Olaizola-Rodrigo, Vira Sharko, Mehran Ashrafi, Jesús del Barrio, Manuel Doblaré, Rosa Monge, Ignacio Ochoa,* and Sara Oliván*

The immune system plays a crucial role in shaping the glioblastoma tumor microenvironment, characterized by its complexity and dynamic interactions. Understanding the tumor-immune crosstalk is essential for advancing cancer research and therapeutic development. Here, a novel multicompartment, barrier-free microfluidic device is presented that overcomes the limitations of existing models by enabling direct tumor-immune interactions without physical barriers, preserving natural immune cell infiltration. This platform supports the independent and simultaneous culture of tumor and immune cells, replicating the healthy-tumoral stroma interface, and allows investigating the effect of matrix stiffness and chemotherapy on both populations. The findings reveal that increased collagen concentration promotes tumor invasiveness while impairing immune cell infiltration. Additionally, temozolomide treatment reduces immune cell motility but enhances anti-tumor immune responses. These insights highlight the critical roles of extracellular matrix mechanics and chemotherapy in tumor progression and immune modulation, establishing this device as a powerful tool for studying glioblastoma-immune dynamics and evaluating therapeutic strategies.

15 months.^[1] The standard treatment regimen, in which Temozolomide (TMZ) is the chemotherapeutic agent used, has remained unchanged for nearly two decades.^[2] However, nearly half of the patients develop resistance to treatment,^[3] primarily due to the high intra- and inter-tumoral heterogeneity that characterizes this tumor. This heterogeneity is strongly driven by its dynamic tumor microenvironment (TME), where surrounding immune cells significantly contribute to tumor aggressiveness and progression.^[4,5] This intricate interaction between the immune system and the tumor goes beyond the cell types involved, as it is strongly influenced by the architecture of the ECM in which it takes place. However, the role of ECM in modulating the immune response in GBM is often overlooked in conventional in vitro models.

The ECM, a complex network of components including collagen, laminin, and hyaluronan, is a crucial element in

maintaining the structural and functional stability of tissues. In the context of GBM, the ECM is not merely a structural scaffold but actively contributes to tumor progression. GBM cells can remodel the ECM, increasing its stiffness through

1. Introduction

Glioblastoma (GBM) is the most prevalent malignant brain tumor in adults, characterized by a median survival of only

C. Bayona, C. Olaizola-Rodrigo, V. Sharko, M. Ashrafi, M. Doblaré, I. Ochoa, S. Oliván
Tissue Microenvironment (TME) Lab
Aragón Institute of Engineering Research (I3A)
University of Zaragoza
Zaragoza 50018, Spain
E-mail: iochgar@unizar.es; soligar@unizar.es

C. Bayona, V. Sharko, M. Ashrafi, M. Doblaré, I. Ochoa, S. Oliván
Institute for Health Research Aragón (IIS Aragón)
Zaragoza 50009, Spain

C. Olaizola-Rodrigo, R. Monge
BEOnChip S.L.
Zaragoza 50018, Spain

J. del Barrio
Centro de Investigación Biomédica en Red en Bioingeniería
Biomateriales y Nanomedicina (CIBER-BBN)
Madrid 28029, Spain

M. Doblaré, I. Ochoa
Instituto de Nanociencia y Materiales de Aragón (INMA)
CSIC-University of Zaragoza
Department of Organic Chemistry
Zaragoza 50009, Spain

The ORCID identification number(s) for the author(s) of this article can be found under <https://doi.org/10.1002/sml.202409229>

© 2025 The Author(s). Small published by Wiley-VCH GmbH. This is an open access article under the terms of the [Creative Commons Attribution-NonCommercial](https://creativecommons.org/licenses/by-nc/4.0/) License, which permits use, distribution and reproduction in any medium, provided the original work is properly cited and is not used for commercial purposes.

DOI: 10.1002/sml.202409229

the secretion of fibrous proteins like collagen.^[6] This stiffening not only promotes tumor aggressiveness but also impedes the efficacy of chemotherapeutic agents and suppresses immune surveillance.^[7] Areas of increased ECM density are often associated with reduced T-lymphocyte infiltration, a phenomenon observed in both human and animal models.^[8] These ECM-driven barriers have a significant impact on the efficacy of both chemotherapy and immunotherapy, underscoring the need to incorporate ECM dynamics into in vitro preclinical models to better understand the physical and biochemical contributions of the ECM to tumor-immune interactions.

Moreover, although TMZ's cytotoxic effects on GBM cells are well-characterized, its impact on the immune system remains poorly understood. Evidence suggests that TMZ exhibits a dual role in modulating immune responses, depending on the dose and mode of administration.^[9] On one hand, TMZ induces lymphopenia and myelosuppression, significantly impairing immune function.^[10,11] On the other hand, it has been suggested that TMZ may enhance anti-tumor immunity by promoting immunogenic tumor cell death, potentially acting as an adjuvant to immune-based therapies.^[9] This duality highlights the complex relationship between TMZ treatment, tumor progression, and immune modulation, emphasizing the importance of understanding its broader effects within the TME.

Recreating these elements in vitro represents a complexity that most existing co-culture models are unable to overcome. These models often fail to accurately simulate key elements of the TME, such as ECM gradients and structural dynamics. Traditional 2D models lack the physiological relevance of ECM interactions, while 3D models, such as organoids or tissue slices, suffer from limitations related to high variability, short lifespan, and limited reproducibility.^[12,13] Moreover, these models lack important physical forces, such as shear stress, which influence immune cell migration.^[14] In recent years, organ-on-chip (OOC) technology has emerged to address these limitations, revolutionizing the field of tissue engineering by enabling the recreation of in vivo-like microenvironments, crucial for studying complex biological interactions and disease mechanisms.^[15–17] However, while OOC models have seen significant progress, the incorporation of the immune system remains a relatively recent development.^[18–20] These models offer a unique opportunity to study immune system functions and their modulation by tumors, especially in inaccessible types such as GBM.

Current OOC models that investigate immune-tumor interaction employ designs with chamber separations that limit the full interaction between cell populations. Artificial barriers can alter the behavior of tumor and immune cells, such as their natural direction of movement when infiltrating into tissues, thereby limiting the accuracy of these models.^[21–25] In addition, most of the current devices are made of polydimethylsiloxane (PDMS), a material limited by its permeability to gases and its non-specific absorption of molecules. To address these limitations, an alternative approach that lacks artificial barriers and uses cyclic olefin polymers (COP) and copolymers (COC) was previously developed, offering biocompatibility, transparency, and impermeability,^[26–28] but only consisting of a single central hydrogel chamber.^[29,30] However, the co-culture of multiple cell populations requires more intricate and compartmentalized devices rather than a single chamber model. In response, this study introduces a novel

device consisting of a complete interconnected three-chamber system that ensures robust interaction between cell populations while also allowing for the continuous renewal of nutrients, oxygen and the administration of drugs. In this study, we focus on exploiting the device design for recreating the interactions between immune cells and GBM in a complex TME (Figure 1). By achieving independent co-culture of peripheral blood mononuclear cells (PBMCs) and U251-MG GBM-derived cell line, we can investigate the impact of ECM stiffening, modulated by collagen concentration, and TMZ treatment on immune cell infiltration in a controlled setting.

2. Experimental Section

2.1. Microfluidic Device Design and Fabrication

The fabrication method employed for manufacturing the device follows the procedure presented in previous work,^[29] with specific adjustments to the device design and the mask. The fabrication technique involved initially cutting the materials using a plotter machine (FC8600-60Wide Vinyl Cutter, Graphtec) to create both the channels and the base with the dimensions that can be seen in Figure 2. Concurrently, the injection-molded part was drilled (OP-TIDRILL B13 BASIC) to create the inlets and outlets of the three central chambers using a 1 mm diameter drill bit. After obtaining all the components of the device (Figure 2A), surface treatment based on oxygen plasma (0.4 mbar, 100 W (50%), 30 s) was performed, turning the lateral chambers in contact with the lateral channels (chamber 1 and 3) hydrophilic. For this purpose, a mask with delineated side chambers was used (Figure 2B). The mask pattern has enabled the modification of the device geometry, achieving three designs with the following dimensions: the standard 2 × 4 mm, and two additional geometries of 2 × 2 mm and 2 × 8 mm (Figure 2H). Following the surface treatment, the bonding process was executed through thermocompression bonding. This involves using the hot embosser (Digital Combo Heat Press, Geo Knight) and a two-step process: first, attaching the base to the channels, and subsequently bonding the entire assembly to the injection-molded part. The final device consists of a multi-compartmentalized design with three central chambers and two lateral channels, with all sections interconnected.

2.2. Validation of the Device

The hydrogel mixture was prepared first, according to the required collagen concentration to simulate biological conditions. Hydrogel components were added to an Eppendorf on ice following the order: sterile distilled water, 10x PBS (Cytiva, SH30258.01), 1N NaOH (Sigma, 655104), high-density collagen type I from rat tail (Corning, 354236) and DMEM medium. Green FluoSpheres diluted in the medium 1/100 (Invitrogen, F8811) were added to the mixture for visualization. The hydrogel was kept on ice during preparation to avoid polymerization, and a volume of 10 μL was seeded first on each of the two lateral chambers (Chambers 1 and 3). Then, the device was placed into an incubator (37 °C and 5% CO₂) for 15 min to polymerize, turning them every 5 min to achieve a homogeneous distribution of

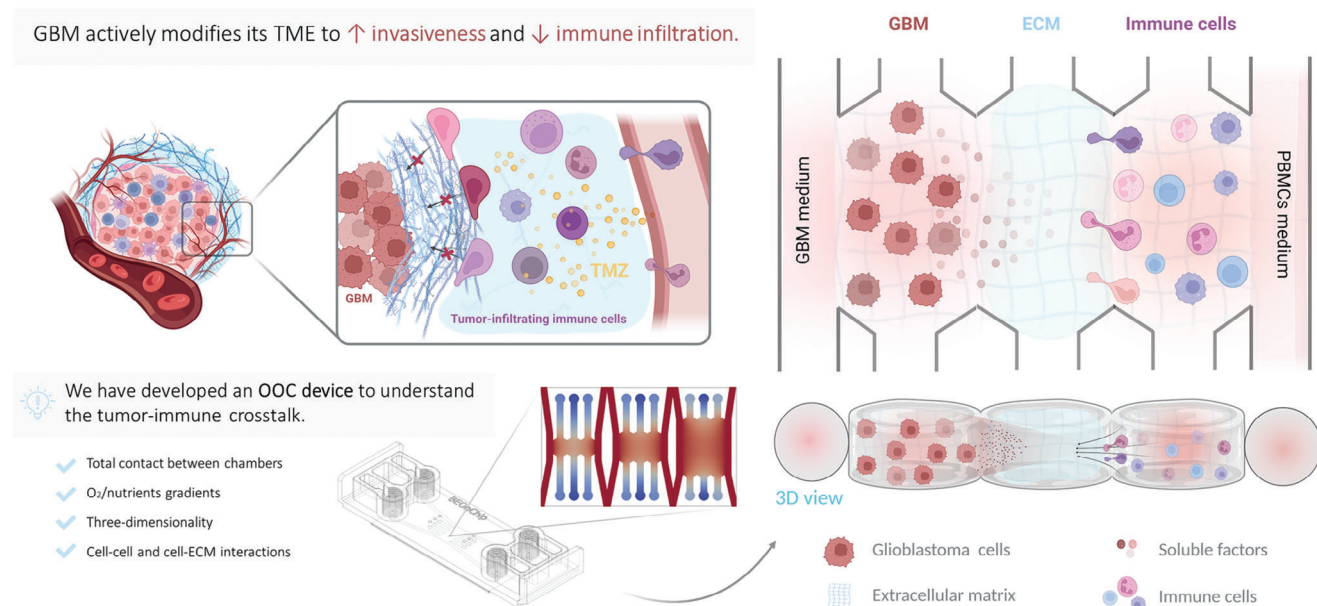


Figure 1. Schematic representation of the TME in GBM and its recreation in this study using a microfluidic device. GBM is known to modify its TME in several ways, including the stiffening of the surrounding ECM. This matrix stiffening exerts a dual pro-tumoral effect *in vivo*: it enhances tumor cell invasiveness while hinders immune cell infiltration into the tumor. Reproducing these complex interactions *in vitro* is challenging. To address this problem, we developed a microfluidic device that mimics these processes, enabling the study of ECM stiffening and T effects on both the tumor and the immune system.

FluoSpheres. After lateral chamber polymerization, the central chamber (Chamber 2) was seeded with the same collagen gel mixture with Red FluoSpheres diluted 1/100 (Invitrogen, F8809). Lateral channels were filled with 1 $\mu\text{g mL}^{-1}$ Rhodamine B (Sigma-Aldrich, R6626) in PBS or red FluoSpheres. Upon completion of the seeding, the same polymerization process as in the lateral chambers was performed. To conduct the gradient formation study, Rhodamine B was introduced simultaneously through the lateral channels, with a volume of 200 μL per channel (Figure 2F). Collagen concentrations of 4 mg mL^{-1} in chamber 1 and 2 mg mL^{-1} in chamber 3 were added. The concentration in central chamber 2 varies between 2 and 4 mg mL^{-1} .

2.3. Computational Simulations

A computational fluid dynamics analysis was conducted to study multiple parameters in the device, focusing on the multiphysics dynamics of the transport of oxygen and fluid flow. The simulations were performed using the FEniCS open-source software package,^[31] which facilitated the implementation of finite element methods to discretize and solve the coupled equations relevant to the study. Fluid movement in the devices was modelled using Navier-Stokes equations for the channels and the Darcy equation for fluid movement in porous media within the chambers. The transport of oxygen was simulated by solving a mass transfer equation, addressing both diffusion and convection mechanisms within the devices. The “Computational Simulation- Fluid Dynamics” section in Supporting Information include details on these aspects of the simulation.

Incorporating the dynamic behavior of a microfluidic device placed on a rocker into our simulations required precise mod-

elling of the device’s response to tilting (movement can be seen in Figure 2J). This was achieved by implementing equations that describe the relationship between the flow rate, hydraulic resistance, and pressure changes as the device oscillates. Pressure, velocity and shear stress were calculated by applying several tilting angles for rocker (2.5°, 5°, 7.5°, 10°, 12° and 15°). In these simulations, the ambient oxygen concentration at the boundaries was maintained at 18%, corresponding to 5.665 $\times 10^{-6}$ mol mm^{-3} of oxygen, consistent with laboratory conditions. The mathematical deduction is detailed as follows.

The flow rate Q through the microfluidic channels was calculated using the formula $Q = \Delta P/R$, where R represents the hydraulic resistance, formulated as:^[32]

$$R = \frac{12\mu L_c}{w_c h_c^3 \left(1 - 0.63 \frac{h_c}{w_c}\right)} \quad (1)$$

This resistance considered the viscosity of the medium, μ , and the geometry of the channel ($L_c = 42.6$ mm, $h_c = 0.2$ mm and $w_c = 1$ mm). The pressure difference ΔP driving the flow was given by $\Delta P = \rho g \Delta h$ with Δh representing the vertical displacement due to the tilt, influenced by the density of the fluid (ρ) and acceleration due to gravity (g). The heights of the fluid columns at the inlet (h_{r1}) and outlet (h_{r2}) were described by sinusoidal functions of time t , reflecting the tilting motion:

$$h_{r1}(t) = \frac{\pi}{12} L_c \sin\left(2\pi \frac{\text{rpm}}{60} t\right) \quad (2)$$

$$h_{r2}(t) = \frac{\pi}{12} L_c \sin\left(2\pi \frac{\text{rpm}}{60} t + \pi\right) \quad (3)$$

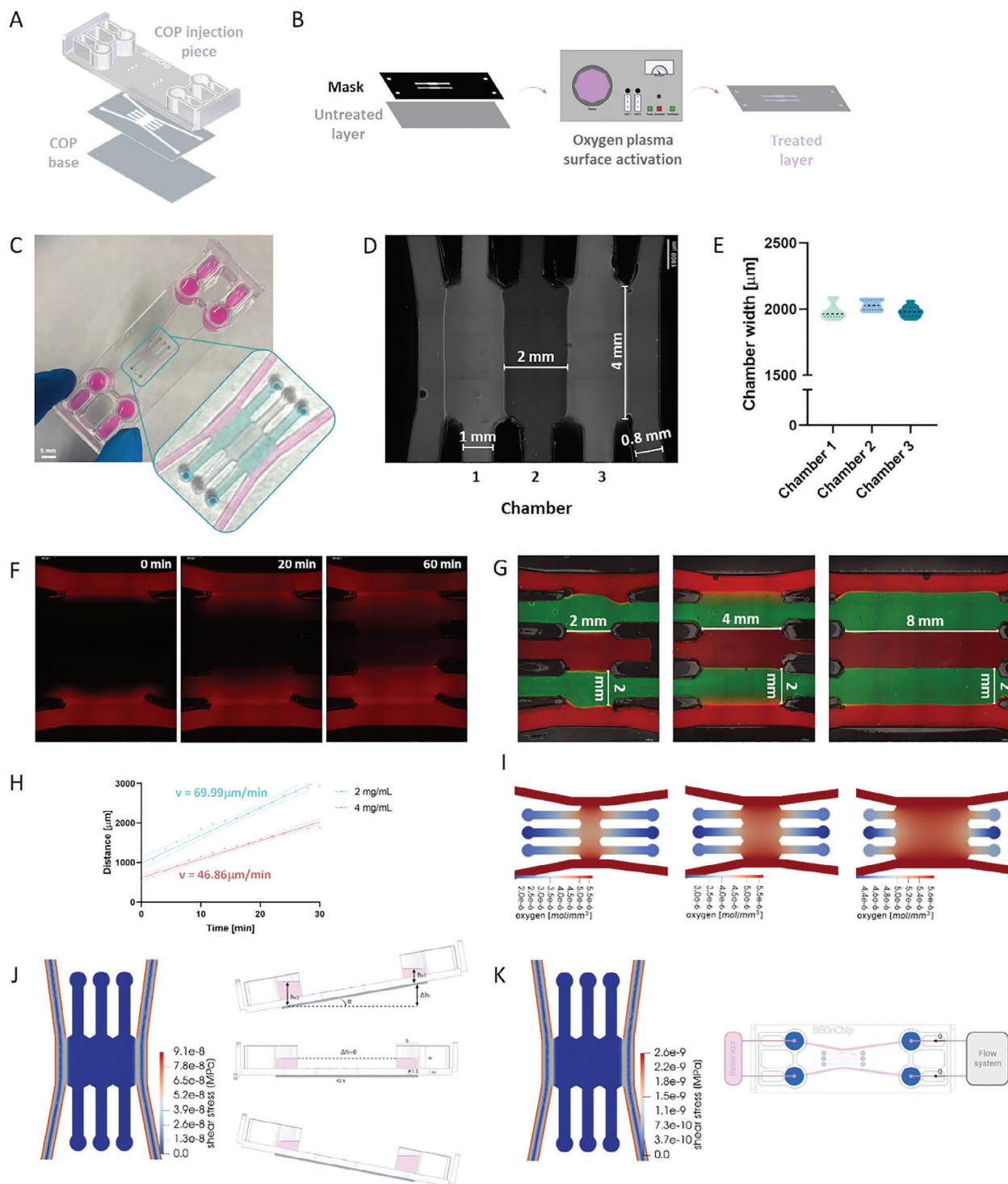


Figure 2. Microfluidic device fabrication and validation. A) Exploded view of the device. B) Mask and surface treatment steps. C) Multicompartmentalized barrier-free device seeded with collagen I gel and dyes. Scale bar represents 5 mm. D) Bright-field image of the three chambers along with device measurements. E) Graph displaying statistical data on the width measurements of the central chambers in 10 devices, obtained using the Leica DMI-8 (Thunder) microscope. F) Rhodamine B diffusion over time along the central chambers seeded with the following collagen hydrogel concentrations: 4 mg mL⁻¹ in chamber 1 and 2 mg mL⁻¹ in chambers 2 and 3. G) Customizable device: 3 different designs for the same fabrication technique, seeded with hydrogel and fluorospheres in chambers and rhodamine through lateral channels. H) Velocity curves for the diffusion of rhodamine through 2 mg mL⁻¹ (blue) and 4 mg mL⁻¹ (red) collagen hydrogel concentration. Measurements made in the lateral chambers of rhodamine diffusion studies shown in image F. I) Oxygen diffusion profiles for 120 min. Three geometries are shown with the collagen concentration distribution 4-2-2 mg mL⁻¹. J) Computational simulation showing shear stress values for (J) rocker motion (in this case, for an angle of 15°) and K) flow studies (in this case, for a flow rate of 5 μL min⁻¹).

A rotation speed of 5 rpm was considered for this study. The velocity at the inlets and outlets was computed using the formula: $velocity_{inlet/outlet} = Q/A$ where $A = h_c \times w_c$ was the cross-sectional area of the inlets or outlets. The pressure at the outlets (and similarly at the inlets when applicable) was set to zero: $pressure_{outlet/inlet} = 0$. The tilting motion of the rocker introduced a dynamic element to the boundary conditions. When tilted upward at the inlets, the fluid experienced an increased hydraulic head, altering the flow rate Q due to gravitational effects and thus changing the velocity according to the above formula. When tilted downward at the outlets, the fluid was aided by gravity, allowing it to exit more freely, justifying the zero-pressure boundary condition.

For flow pump calculations, flow rates of (5, 10, 50, 100, 200 and 600 $\mu\text{L min}^{-1}$) were used (see the “Computational simulations- Fluid Dynamics” section in Supporting Information).

2.4. Cell Culture

GBM-derived cell line U-251 MG (Sigma, 09063001) was stably transduced with a green fluorescent protein (GFP)-expressing lentiviral vector, kindly provided by Dr. Prats, University Paul Sabatier, Toulouse, France. Cells were cultured in high Glucose Dulbecco's Modified Eagle's Medium (DMEM) (Lonza, BE12-614F) supplemented with 10% (v/v) Fetal Bovine Serum (FBS) (Gibco, 10270-106), 1% Penicillin/Streptomycin (Lonza, DE 17-602E) and 1% Glutamine (Lonza, H3BE17-605E/U1f). Cells were grown in adherent 75 cm^2 T-flasks and maintained in an incubator at 37 °C and 5% CO_2 . Once 70–90% confluence was reached, cells were trypsinized to achieve the necessary cell density for chip seeding.

PBMCs were isolated from whole blood from healthy donors provided by the Biobank of the Aragon Health System (National Registry of Biobanks B. B.0000873) (PT23/00146), integrated in the Platform ISCIII Biobanks and Biomodels. All samples were processed following standard operating procedures with the appropriate approval of the Ethics and Scientific Committees. First, whole blood was diluted 1:1 with PBS (Gibco, 14-200-075). Lymphoprep (Stem Cell, 07801) was added to a 50 mL falcon tube (in a volume equal to the volume of diluted blood). The blood was gently placed on top. The system was centrifuged at 500 g for 30 min with no brake at room temperature. The immune fraction (PBMCs) was transferred to a new falcon tube, washed with DPBS and centrifuged at 400 g for 5 min at room temperature. The pellet was incubated in red blood cells lysis buffer (Invitrogen, 00-4333-57) for 10 min and washed until the pellet was completely white. Finally, PBMCs were resuspended in RPMI medium (Gibco, 11875093) supplemented with 10% FBS and 1% Penicillin/Streptomycin.

2.5. Cell Seeding on the Microfluidic Device

The chips were UV sterilized beforehand. All reagents were kept on ice. First, cells were trypsinized and resuspended in a calculated volume of supplemented DMEM medium to achieve the desired concentration of cells in the final hydrogel solution. The

hydrogel components were added to an Eppendorf on ice following the aforementioned order: sterile distilled water, 10x PBS, 1N NaOH, high-density collagen type I from rat tail and the cell suspension. U-251 MG cells were seeded at a concentration of 40 million mL^{-1} and PBMCs were seeded at 20 million mL^{-1} . Prepared mixture was well-resuspended on ice and seeded with a volume of 10 μL into the right (chamber 1) and left (chamber 3) chambers respectively. The chip was then placed in the incubator at 37 °C and 5% CO_2 for 20 min for complete polymerization of the collagen hydrogel and turned up and down during that time to achieve a homogeneous distribution of cells over the entire height of the chip. Once polymerized, pre-warmed supplemented DMEM growth medium for GBM cells and supplemented RPMI medium (with 100 IU mL^{-1} Interleukin-2 (IL-2)) for PBMCs were added through the lateral channels to gradually provide nutrients to the cells in the central chamber. Then, the central chamber was seeded with 10 μL of collagen hydrogel without cells and was kept in the incubator until complete polymerization as explained above. To maintain the cell culture, the chips were placed in a bi-directional rocker (IKA, 4003000) with an angle of 15°, inside the incubator (37 °C, 5% CO_2).

2.6. Hydrogel Rheological Measurements

Rheological measurements were performed on three independent samples using a rheometer (Haake Mars 40) with a parallel plate geometry (gap size: 1 mm, plate diameter: 25 mm). Gels were prepared at 0 °C following the protocol outlined in the previous point of Experimental Section and transferred to the rheometer. Then, the temperature increased from 0 °C to 37 °C, to induce the formation of the hydrogel.

Initially, kinetic measurements were performed, by means of oscillatory rheology (constant amplitude and frequency), to monitor gel formation and ensure sample equilibration. Following kinetic stabilization, frequency and amplitude sweeps were conducted to further characterize the viscoelastic behavior of the gels. The rheological characterization of our gels was completed with a series of amplitude sweeps (see Figure S4, Supporting Information) further validating the stability of the gels.

2.7. Temozolomide Treatment

TMZ (Sigma, T2577) was reconstituted to a concentration of 100 mM in dimethyl sulfoxide (DMSO). The drug was used at 100 μM in co-cultures and applied to the side channels every day for 5 days, replicating the scheme dose in patients. The controls were refreshed with medium containing DMSO at the same concentration (0,1%). Both conditions were supplemented with 100 IU mL^{-1} IL-2.

2.8. Enzyme-Linked Immunosorbent Assay (ELISA)

Immunoenzymatic ELISA assay was performed for interleukin 12 (IL-12) (BD OptEIA, 555183) and tumor necrosis factor alpha (TNF- α) (BD OptEIA, 555212). Levels of growth factors were determined according to the manufacturer's protocol. All samples

were assayed in triplicate, and the mean values of cytokines were considered. Optical density was measured at 450 and 570 nm with the Synergy™ HT microplate reader (Biotek).

2.9. Immunofluorescence

Microfluidic devices with the cells were fixed with 4% paraformaldehyde (VWR, 9713.9010) for 30 min and several washes with PBS were performed. Permeabilization was done with 0.1% Triton X-100 (Merck Sigma-Aldrich, T8787) for 15 min. Phalloidin rhodamine (Invitrogen, R415) was added at $1 \mu\text{g mL}^{-1}$ and incubated overnight at 4°C . Three washes with PBS were performed before visualization.

2.10. Image Analysis

Bright-field and fluorescence images were obtained using a Leica DMi-8 (Thunder) microscope. Images of several Z-planes were taken for each experiment involving PBMCs, ensuring a homogeneous representation of the device height. Subsequently, a plane projection was applied to the final images. All the images were processed and analyzed using Fiji ImageJ software. For PBMCs migration analysis, Fiji ImageJ was used for particle segmentation and cell tracking (TrackMate plugin). For cell tracking, 50 cells of each condition were used for analysis, ensuring that the points correspond to complete trajectories through the time-lapse.

2.11. Statistical Analysis

Data was processed with GraphPad Prism 8 software. Normal distribution was tested by the Shapiro-Wilk test. For parametric comparison, statistical significance was assessed by Student's t-test. Mixed comparisons were made with One or Two-way ANOVA tests, followed by Sidak's multiple comparisons test as a post hoc analysis to identify significant differences between groups. Asterisks represent the significance level (* $p < 0.0332$, ** $p < 0.0021$; *** $p < 0.0002$; **** $p < 0.0001$). Data was shown as mean \pm standard error of the mean (SEM). An $n \geq 3$ was performed for each condition and experiment, and at least 3 distinct regions within a device were analyzed to ensure the reproducibility of the measurements.

3. Results

3.1. Fabrication of a Novel Multicompartment Barrier-Free Microfluidic Device

The development of this device enables precise manipulation of various compounds and stiffnesses in direct contact, removing operational challenges. This advancement is attributed to the surface treatment applied to the device and the customizability of the design. The reproducibility of the device was assessed by measuring the dimensions of the chamber geometry after treatment and comparing them both within and between devices, considering each chamber position (chamber 1,

2, or 3) (Figure 2D,E). For this purpose, 10 devices were evaluated. A 2-way ANOVA test was applied to compare the chamber widths, and no significant differences were found between devices. Additionally, the dimensions of the three chambers within each device were compared, with no statistically significant differences observed. An ordinary one-way ANOVA was conducted to compare the chambers by position across devices. Specifically, the measurements for chamber 1 ($1983 \pm 61 \mu\text{m}$), chamber 2 ($2030 \pm 39 \mu\text{m}$), and chamber 3 ($1982 \pm 43 \mu\text{m}$) showed no significant differences (p -value = 0.0618). Thus, the fabrication process demonstrated high consistency, validating the reproducibility of the technique. Moreover, the manufacturing process allowed for the creation of OOCs with variable chamber sizes (Figure 2H), modifying the chamber length from 2 to 8 mm, resulting in three distinct geometries: 2×2 , 2×4 , and 2×8 mm, which enhanced the versatility of the design and its use for potential applications.

3.2. Validation of the Microfluidic Device

To validate the device, particle diffusion tests and computational simulations were performed. In the case of particle diffusion tests, rhodamine was used to study the effect of ECM stiffening, employing high (4 mg mL^{-1}) and low (2 mg mL^{-1}) collagen concentrations for the ECM matrices (Figure S1, Supporting Information). The device was observed to create a stable and homogeneous diffusion gradient that was consistent across all three chambers. In this gradient experiment, it was also observed that particle diffusion occurred at a greater speed ($69.99 \mu\text{m min}^{-1}$) when the concentration of collagen was lower (as seen in chamber 3, which had a concentration of 2 mg mL^{-1}), and at a slower rate ($46.86 \mu\text{m min}^{-1}$) when the concentration was higher (as observed in chamber 1, which had a concentration of 4 mg mL^{-1}) (Figure 2G).

Regarding computational simulations, diffusion studies of oxygen molecules in different collagen stiffnesses were carried out. No significant differences were observed between the 2 and 4 mg mL^{-1} stiffnesses (Figure 2I; Figure S2, Supporting Information) in the standard geometry device used in this article. However, when data from different geometries were compared, some differences emerged. For the 2×2 mm design, the oxygen diffusion value in the central chamber at 120 min was $4 \times 10^{-6} \text{ mol mm}^{-3}$, for the dimensions 2×4 mm, $4.5 \times 10^{-6} \text{ mol mm}^{-3}$ and, for the 2×8 mm, $5 \times 10^{-6} \text{ mol mm}^{-3}$. The 2×8 mm design exhibited a higher oxygen concentration in the central chamber due to the larger interface with the channels, which facilitates greater oxygen diffusion compared to shorter interface lengths. In each design, the oxygen concentration was higher in the left and right chambers compared to the central chamber. Concerning the standard dimensions (2×4 mm), the oxygen values in the side chambers were $5.5 \times 10^{-6} \text{ mol mm}^{-3}$ and in the central chamber, $4.5 \times 10^{-6} \text{ mol mm}^{-3}$.

Computational simulations were also used to analyze the pressures, velocities and shear stresses inside the device with a rocker flow. Additionally, simulations using a flow pump system were performed to provide values to be considered depending on the flow system and the application (Figure S3, Supporting Information). The presented data is focused on the rocker (used in this

study) or flow configuration in the standard 2×4 mm design under varying conditions (Figure 2J). Values were assigned for the rocker's angle and the flow rate applied through the device's inlets. Specifically, the maximum pressures were ≈ 0.7 , 1.4, 2, 2.8, 3, and 4 Pa at angles of 2.5° , 5° , 7.5° , 10° , 12° , and 15° , respectively. For the flow rates, the pressures increased as follows: 0.11, 0.22, 1.1, 2.2, 4.5, and 14 Pa at rates of 5, 10, 50, 100, 200, and $600 \mu\text{m min}^{-1}$, respectively. In terms of maximum velocities, for the rocker configuration, the measurements were 3, 6, 10, 12, 16 and 20 mm s^{-1} for the same angle values. For the flow rate settings, the magnitude of maximum velocities was recorded at 0.55, 1.1, 5.5, 11, 22, and 70 mm s^{-1} for the same flow rate values. For shear stress (Figure 2J), the rocker configuration yielded values of 1.53×10^{-2} , 3.05×10^{-2} , 4.57×10^{-2} , 6.09×10^{-2} , 7.31×10^{-2} , 9.13×10^{-2} Pa, while the flow configuration showed a wider range of values: 2.57×10^{-3} , 5.14×10^{-3} , 2.57×10^{-2} , 5.14×10^{-2} , 1.03×10^{-1} , and 3.08×10^{-1} Pa.

3.3. Recreation of the Glioblastoma-Immune Microenvironment in the Organ-On-Chip Device

Our three-chamber microfluidic device successfully mimics the infiltration of immune cells into GBM tumors within a 3D ECM (Figure 1). GBM-derived U-251 MG tumor cells were embedded in a 4 mg mL^{-1} collagen hydrogel within the left lateral chamber, receiving nutrients and oxygen from the adjacent channel containing supplemented DMEM. Immune cells, embedded in a 2 mg mL^{-1} collagen matrix, were seeded in the right chamber, receiving supplemented RPMI through the right-side channel.

Cellular behavior within the device, encompassing interactions between GBM and immune cells, is influenced by gradients of oxygen, nutrients, chemotaxis, diffusion, proliferation, and apoptosis, among others. These factors interact to regulate cellular functions *in vivo*. OOC models are able to recreate complex pathophysiological environments and, combined with *in silico* predictions, provide a more complete insight onto these intricate biological processes. In this study, mathematical models developed alongside the *in vitro* platform also demonstrated the strong correlation between GBM and immune system behavior observed both in the device (Video S3, Supporting Information). Using this setup, the effects of ECM stiffening and TMZ treatment on tumor and immune cells were studied, offering a robust platform for exploring the complex tumor-immune interactions.

3.4. Stiffening of the ECM Prevents Infiltration and Migration of Immune Cells Toward the Tumor

In order to study how ECM stiffness affects immune infiltration, the central chamber separating GBM and immune cells was seeded with varying concentrations of 2 and 4 mg mL^{-1} , simulating ECM stiffening *in vitro*.^[33,34] ECM stiffness was modulated by adjusting collagen concentration, as confirmed by rheology studies (Figure S4, Supporting Information). The mean storage modulus, G' , and loss modulus, G'' , measured after gel stabilization in the kinetic study, demonstrated a clear relationship between collagen concentration and stiffness. Specifically,

at 2 mg mL^{-1} , G' was 11.70 ± 1.65 Pa and G'' was 2.03 ± 0.30 Pa, while at 4 mg mL^{-1} , G' increased to 71.09 ± 4.50 Pa and G'' to 11.83 ± 0.61 Pa. These findings confirm that higher concentrated collagen matrices exhibit higher stiffnesses, directly correlating with ECM mechanics, in agreement with previous similar studies.^[33,35,36]

Experiments at baseline, 24 and 48 h showed notable differences between the two stiffnesses (Figure 3). At 24 h, significant differences ($^{***}p < 0.002$) appeared for the maximum distance travelled by the most infiltrating immune cells in a soft versus a dense matrix ($482 \pm 275 \mu\text{m}$ at 2 mg mL^{-1} and $196 \pm 68 \mu\text{m}$ at 4 mg mL^{-1} , $n = 10$ in both cases). This difference became more noticeable after 48 h ($^{****}p < 0.0001$), where it became evident that ECM stiffening greatly affects immune cell infiltration ($1132 \pm 160 \mu\text{m}$ at 2 mg mL^{-1} and $456 \pm 154 \mu\text{m}$ at 4 mg mL^{-1} , $n = 10$ in both cases) (Figure 3B).

Regarding the percentage of cells infiltrating the ECM after 48 h considering different regions (low, medium and highly invasive cells described in Figure S5, Supporting Information), there were significant differences in the infiltration of immune cells into the matrix according to stiffness ($^*p < 0.0332$ for 25, 50 and 75%, $n \geq 3$) (Figure 3C). For the initial region or low invasive cells, there was an apparent difference between cells that infiltrated this region in soft matrices (144 ± 60 cells) versus stiff matrices (37 ± 7 cells). The same was true for the medium invasive cells, where the 2 mg mL^{-1} ECM had a mean number of infiltrating cells of 36 ± 19 , compared to 5 ± 4 for the 4 mg mL^{-1} matrix. Finally, a similar trend occurred in the region furthest from the start or highly invasive region, with 11 ± 3 cells in the soft ECM versus 1 ± 2 cells in rigid ECMs. The concentration of proinflammatory cytokines present according to stiffness showed significant differences in both IL-12 ($^*p < 0.0332$, $n \geq 6$) and TNF- α ($^{**}p < 0.002$, $n \geq 6$) levels. IL-12 appeared to be found at a higher mean concentration in low stiffness ($2.7 \pm 1.9 \text{ pg mL}^{-1}$) than in high stiffness ($0.5 \pm 0.2 \text{ pg mL}^{-1}$) (Figure 3D). TNF- α had a similar trend, although with a greater difference between stiffnesses ($71 \pm 20 \text{ pg mL}^{-1}$ at 2 mg mL^{-1} versus $7 \pm 5 \text{ pg mL}^{-1}$ at 4 mg mL^{-1}) (Figure 3E).

3.5. Tumor Cells Increase their Invasive Capacity in Stiffer Matrices

To study the morphology adopted by GBM-derived U-251 MG cells, staining with fluorescently labelled phalloidin was performed and analyzed by fluorescence microscopy after 5 days of cell culture on-chip (Figure 4). Both cells in soft and stiff matrices expressed F-actin. However, this expression differed depending on the stiffness of the ECM surrounding the tumor. To evaluate the effect of ECM stiffness on U-251 morphology, actin fiber length was analyzed for those invading the central chamber. Tumor cells invading a matrix of 2 mg mL^{-1} appeared to have fewer and shorter cytoskeletal extensions ($84 \pm 19 \mu\text{m}$, $n \geq 8$), whereas tumor cells invading a denser matrix of 4 mg mL^{-1} appeared to extend more and possess a more invasive morphology ($226 \pm 114 \mu\text{m}$, $n \geq 8$). In addition, more cells in the stiffer matrix (3 ± 1 cells in 2 mg mL^{-1} ECM, 23 ± 11 cells in 4 mg mL^{-1} ECM, $^*p < 0.03$, $n \geq 3$) moved further away and invaded a more distant area from their original chamber after 5 days of the

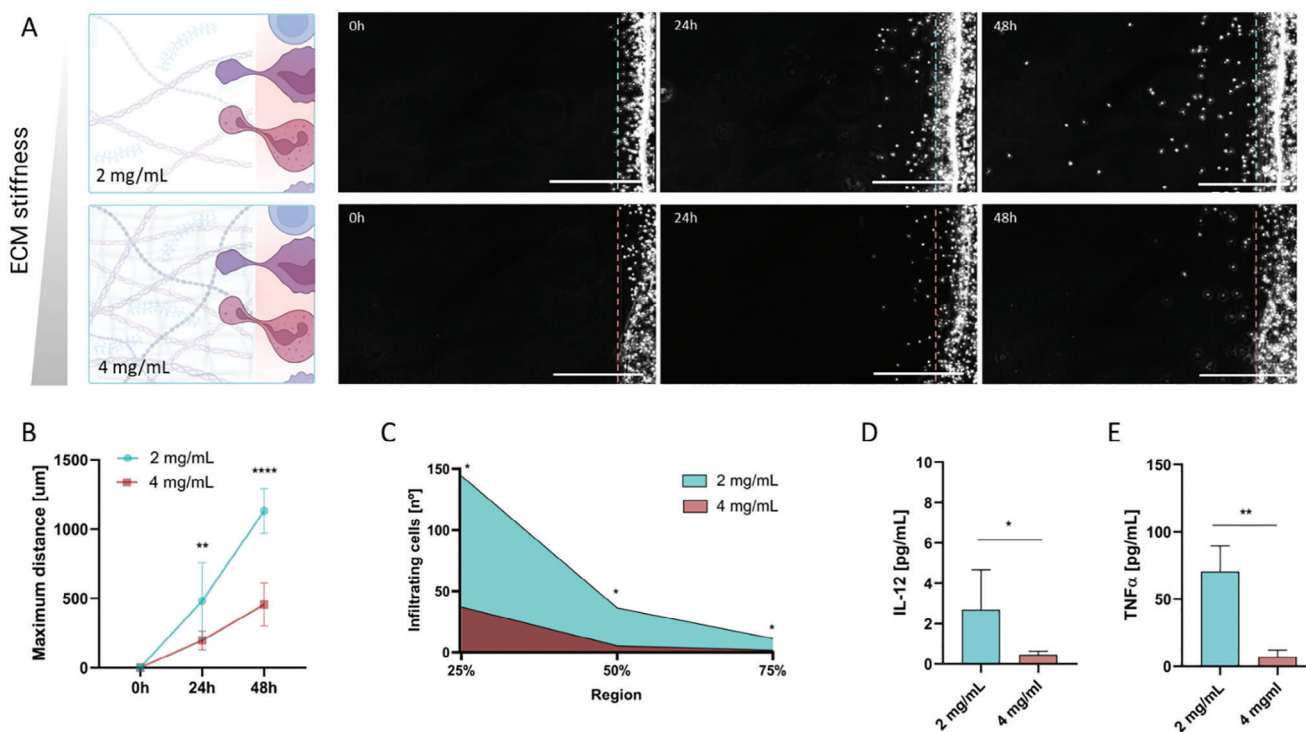


Figure 3. ECM stiffness hinders the infiltration and arrival of immune cells to the tumoral core. A) Images taken under phase contrast of immune cell infiltration (white dots) into the ECM of 2 mg mL⁻¹ (top) and 4 mg mL⁻¹ (bottom) toward GBM cells (left side, not shown). B) Plot of the maximum distance travelled by immune cells into each stiffness at different times. C) Cell count density of infiltrating PBMCs at 48 h in different regions of the ECM, represented as a percentage from the initial point (25%) to the further region (75%). D) IL-12 concentration according to stiffness E) TNF-α concentration according to stiffness. **p* < 0,0332; ***p* < 0.0021; *****p* < 0.0001. Scale bar corresponds to 500 μm.

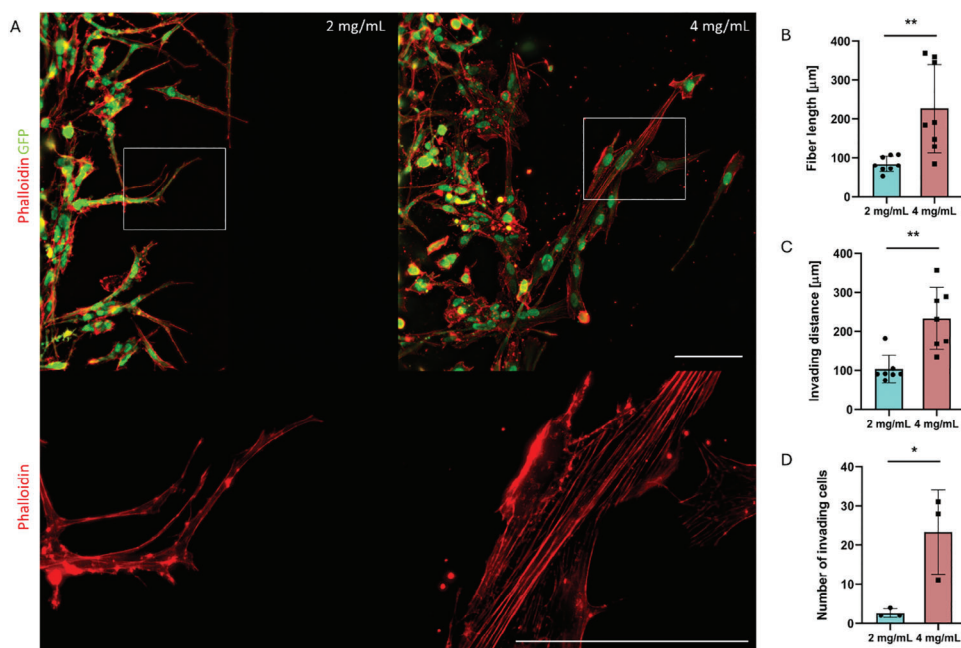


Figure 4. GBM cells acquire a more invasive morphology in stiffer matrices. A) Images taken under fluorescence microscopy of F-actin expression (red) in U-251 MG GFP-transfected cells according to ECM stiffness (2 mg mL⁻¹ on the left; 4 mg mL⁻¹ on the right). The upper images of both stiffnesses show the cell morphology in the region of the central chamber adjacent to the tumor chamber. The lower images show a magnification of the upper images. The graphs correspond to B) the fiber length measurements, C) the invasion distance of cells and D) the number of invading tumor cells in the different stiffnesses. **p* < 0,0332; ***p* < 0.0021. Scale bar corresponds to 100 μm.

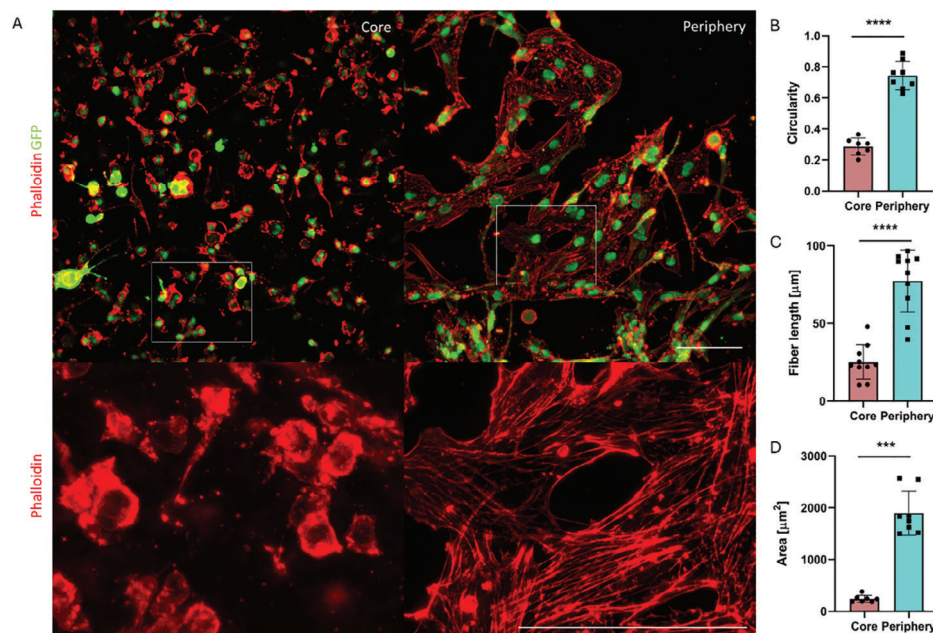


Figure 5. The morphology of GBM cells varies according to the tumor region, having an amoeboid morphology in the center versus a mesenchymoid morphology in the invasive periphery. A) Images taken under fluorescence microscopy of F-actin (red) expression in U251-MG. The left image shows the central region of the tumor, while the invasive region of the periphery is shown on the right. The lower images show a magnification of the upper images in both regions. The graphs show significant differences in circularity B), fibrillar length C) and cell area of central versus invasive tumor cells D). *** $p < 0.0002$; **** $p < 0.0001$. Scale bar corresponds to 100 μm .

experiment ($104 \pm 36 \mu\text{m}$ in 2 mg mL^{-1} ECM, $234 \pm 79 \mu\text{m}$ in 4 mg mL^{-1} ECM, ** $p < 0.021$, $n \geq 7$).

3.6. Tumor Cells Acquire an Invasive Mesenchymal-Like Morphology in the Periphery Region

The expression of F-actin also differed depending on whether it was the center of the tumor or the periphery (Figure 5). Tumor cells were seeded in a stiffer matrix compared to immune cells (4 and 2 mg mL^{-1} , respectively), as tumors are known to stiffen the surrounding ECM. Cells in the center of the tumor were observed to have an amoeboid morphology with a statistically significant circularity compared to the invasive cells in the periphery, which displayed a more elongated and expanded mesenchymoid-like morphology (**** $p < 0.0001$, $n \geq 8$). In addition, cells in the core appeared to express less F-actin and had a disordered fiber organization, in contrast to cells in the periphery, which appeared to have reorganized the cytoskeleton, showing higher levels of F-actin. This reorganization in the periphery also causes the cytoplasm to expand, resulting in larger cell areas than found in the center (*** $p < 0.001$, $n \geq 8$). Moreover, a greater length of actin fibers was observed in the mesenchymoid-like cells of the periphery, with fibers 3 times longer than in the tumor center (**** $p < 0.0001$, $n \geq 10$).

3.7. Temozolomide Treatment Decreases Infiltration of Immune Cells Into the Tumor

To study the modulatory effect of TMZ on the immune system, OOC devices were seeded with GBM-derived U-251 MG cells and

PBMCs in the left and right chambers, respectively, leaving the central chamber with a collagen hydrogel concentration of 2 mg mL^{-1} . This concentration was selected based on the results of previous stiffness experiments, which demonstrated that PBMCs exhibited adequate behavior in the 2 mg mL^{-1} matrix. Both cell types were treated with standard TMZ treatment, consisting of one dose per day for a total of 5 days, and drug-free controls were used to measure the differences (Figure 6). The infiltration experiments showed significant differences in the total number of infiltrating cells after 48 h (**** $p < 0.0001$, $n \geq 6$), where it also showed the largest difference from the control (Figure 6B). Regarding the percentage of infiltrating cells considering different regions, the central matrix was divided into three zones as previously: highly, medium and low invasive cells (Figure S5, Supporting Information). The most infiltrating cells (highly invasive cells from Figure 6D) showed notable differences from 72 h onward between control and treated (** $p > 0.002$, $n \geq 6$). The less infiltrating cells closer to the PBMCs chamber (Figure 6F) showed a similar trend compared to the total infiltrating cells, as these were the most numerous and therefore contribute the most to the total infiltration data. On the other hand, the invasive front, referring to the area of the central chamber occupied by the PBMCs as they infiltrate (Figure 6C), showed significant differences during the first two days (** $p > 0.002$, $n \geq 6$). This trend changed at 72 h, when cells from both conditions reached the tumor cell chamber.

The motility of PBMCs was also studied with 10 min time-lapse of each condition (Figure 6G). Cell tracking showed significant differences (**** $p < 0.0001$, $n \geq 30$) in the mean cell velocity, being higher in the control ($4.7 \pm 1.6 \mu\text{m 30s}^{-1}$) than in the TMZ devices ($2.3 \pm 0.4 \mu\text{m 30s}^{-1}$) (Figure 6H,J,K). The displacement of immune cells was also reduced with TMZ application

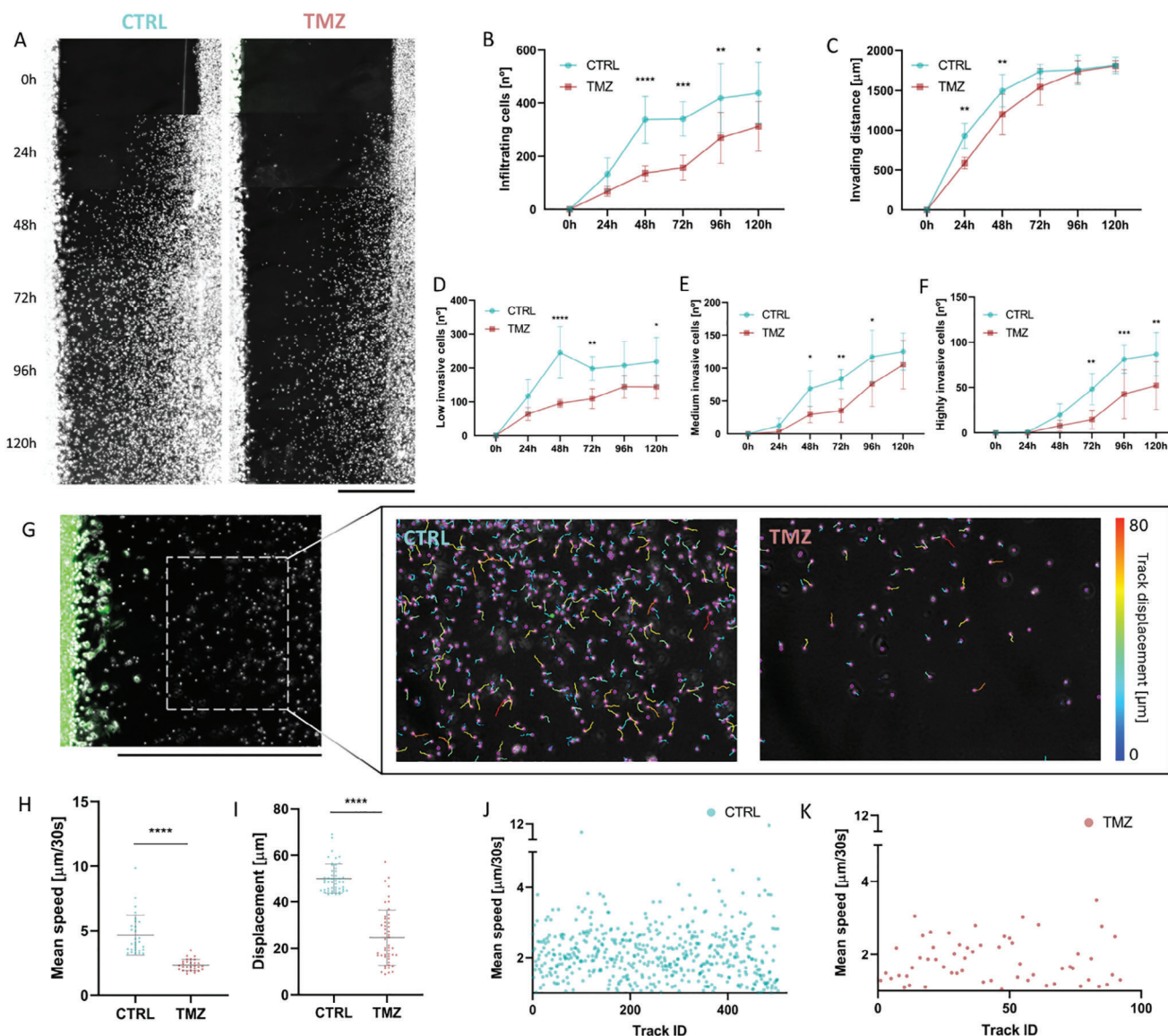


Figure 6. TMZ slows the infiltration of immune cells into the tumor. A) Central chamber with immune cells (white, right) moving toward the tumor (left). Images show a control device and TMZ over 5 days. Graphs of invasive cells B), invasive front distance C) and highly D), medium E) and low F) infiltrating cells. G) Time-lapse images and the region chosen for cell tracking analysis. The control and TMZ show the trajectories obtained with TrackMate plugin (Fiji ImageJ), classified by color according to their displacement (red for longer trajectories, or greater displacement, and blue for shorter trajectories). More information can be found in Supplementary videos 1 and 2. Graphs of the average cell velocity H), the displacement I) and the individual velocity points in the control J) and TMZ (K). * $p < 0,0332$; ** $p < 0,0021$; *** $p < 0,0002$; **** $p < 0,0001$. Scale bar corresponds to 1000 μm .

(* $p < 0,0001$, $n \geq 30$), from $50 \pm 6 \mu\text{m}$ in the control to $25 \pm 12 \mu\text{m}$ after TMZ.

3.8. Temozolomide Induces an Early Activation of Pro-Inflammatory Cytokines and Exhibits no Cytotoxic Effect on Immune Cells

To elucidate the ability of TMZ to modulate the immune system, ELISAs of the cytokines IL-12 and TNF- α were performed at different time points during the experiment. At 48 h, IL-12 showed a significant increase (* $p < 0,002$, $n \geq 6$) in the media from the

immune channel of the devices with TMZ ($20 \pm 15 \text{ pg mL}^{-1}$) versus controls ($1,7 \pm 1,8 \text{ pg mL}^{-1}$) (Figure 7A). In the case of TNF- α a similar trend (* $p < 0,002$, $n \geq 6$) occurred between the immune channels of devices with TMZ ($173 \pm 91 \text{ pg mL}^{-1}$) versus control ($25 \pm 12 \text{ pg mL}^{-1}$) (Figure 7B). On the other hand, at 120 h of culture, the significant differences in both cytokines disappeared if we compare the control with the TMZ (Figure 7C,D).

To test whether TMZ could have a cytotoxic effect on PBMCs, calcein, propidium iodide and Hoechst staining was performed at day 5 on control and TMZ devices (Figure 7E), $n \geq 3$. The aim was to study the percentage of cell death with respect to total cells in different regions of the device. No significant differences in cell

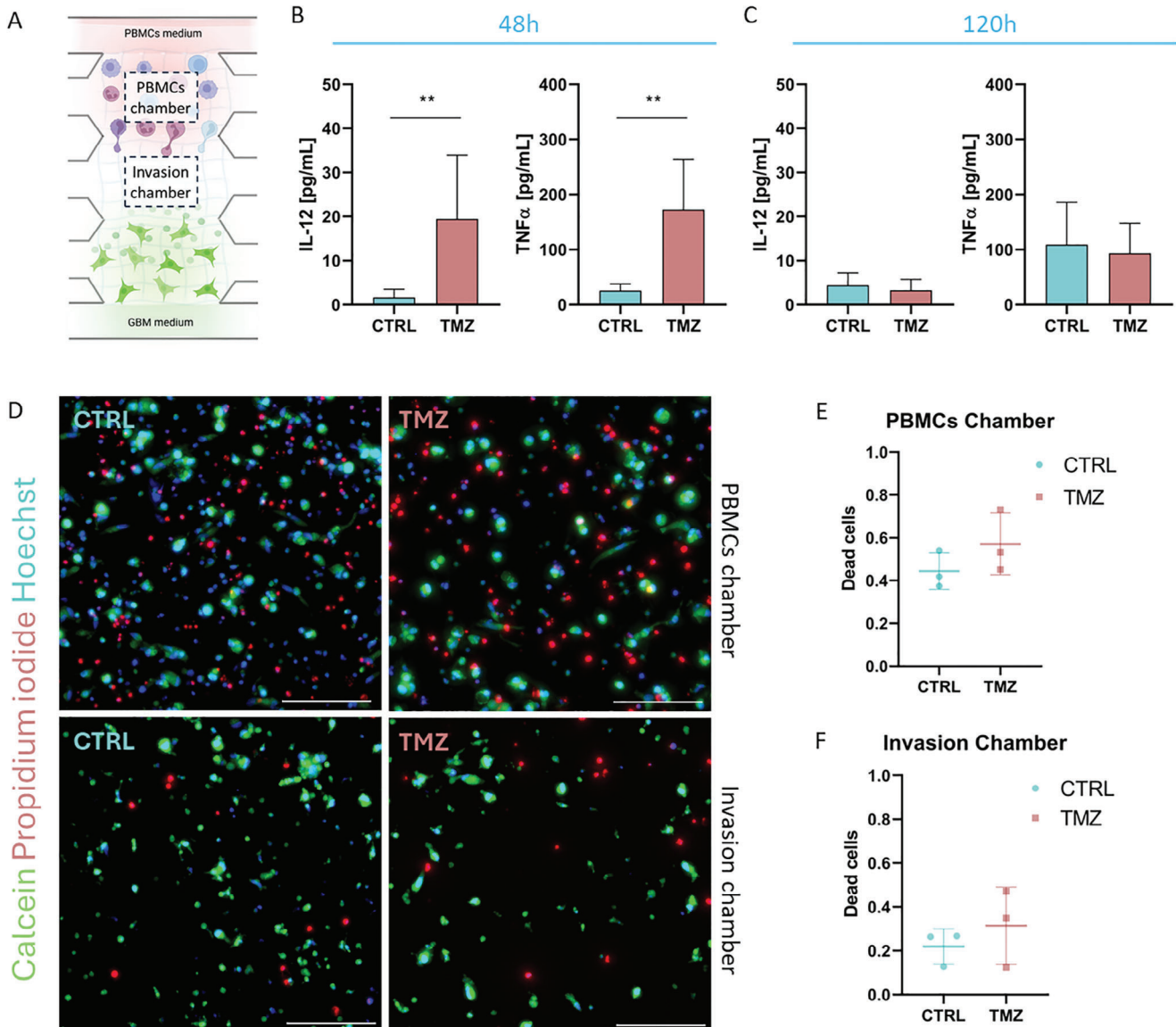


Figure 7. TMZ induces activation of pro-inflammatory cytokines and does not cause cell death in immune cells. A) Representative scheme of PBMCs chamber and Invasion chamber. Plots of ELISAs performed on control and TMZ devices at 48 h B) and 120 h C) of IL-12 and TNF- α . D) Fluorescence images showing the chamber where PBMCs are seeded at baseline (top) in control (left) and TMZ (right), and the central chamber where infiltration occurs (bottom) in control (left) and TMZ (right) after 5 days of experiment. Cells are stained with calcein (green), propidium iodide (red) and Hoechst (blue). Plots of the percentage of dead cells over total cells in the PBMC chamber E) and the central invasion chamber F). ** $p < 0.0021$. Scale bar corresponds to 200 μ m.

death due to TMZ were found in either the chamber where the PBMCs were initially seeded (Figure 7F) or in the central chamber where immune infiltration was observed (Figure 7G). However, there was a slight significance ($*p < 0.03$) in the percentage of dead cells between PBMCs and the invasion chamber in the untreated condition.

4. Discussion

The immune system is a key element within the GBM TME, a highly dynamic and heterogeneous network shaped by interactions between tumor and immune cells. The surrounding scaffold

and physicochemical gradients are equally crucial for these interactions,^[37,38] emphasizing the need for models that accurately replicate such complexity.^[39] In this study, we present a novel microfluidic platform that successfully captures the multifaceted dynamics of cancer-immune interactions in GBM.

Microfluidics has emerged as a promising approach to recreate cancer-immune crosstalk in a controlled, reproducible environment.^[40] However, existing designs often introduce barriers, such as membranes,^[41,42] pillars^[43,44] and phaseguides,^[45,46] which disrupt immune cell infiltration and limit their ability to mimic in vivo conditions. Other techniques, such as laminar flow patterning, while they remove physical barriers, are constrained

by their incompatibility to create specific geometries.^[47,48] Additionally, methods like photopatterning enable the creation of desired geometries through laser processing. However, the laser can damage the hydrogel's properties, interfering with natural cell-to-cell contact and restricting cell movement.^[49,50] Our design overcomes these challenges by eliminating physical barriers and compartmentalizing co-cultures into independent chambers, facilitating interaction between immune and tumor populations. Besides, the adaptable design allows for geometric modifications, facilitating its use in diverse experimental settings based on specific needs, including reagent quantities, cell concentration and available interaction surface. Additionally, this design enables the generation of oxygen-independent chemotactic gradients by modulating chamber stiffness, critical for studying immune cell migration, as random migration occurs in the absence of such gradients.^[14] Beyond gradient generation, intrinsic device values of shear stress, oxygen diffusion, velocity and pressure can also significantly impact immune cell behavior.^[51] While shear stress is essential for guiding immune cell migration, values exceeding physiological ranges—normally 0.05–1 Pa for leukocytes—may impair immune cell function.^[52] Accordingly, as evidenced by computational data, shear stress levels generated by the rocker in the study are suitable for the immune system. Additionally, a flow pump system can contribute to a wider range of shear stress values if needed for other applications, such as vascular endothelial cells,^[53–55] metastatic cancer cells^[56] or intestinal epithelial cells.^[57]

From a biological perspective, our device enables the independent culture of GBM and immune cells within a complex 3D matrix, preserving physical separation to facilitate the study of interactions induced by ECM modifications or TMZ treatment. GBM is known for its capacity to mechanically alter its microenvironment by increasing the density of the ECM, especially through the secretion of collagen fibers. This can compromise vascular integrity leading to increased hypoxia, which in turn promotes tumor invasiveness and malignancy.^[58,59] In our model, ECM stiffness was modulated by varying collagen concentration. This approach not only alters stiffness but also introduces changes in other parameters, such as collagen ligand density and integrin signaling engagement, which are intrinsic to the biological system being modeled.

GBM cells exhibit more invasive morphology and behavior in stiffer matrices (4 mg mL⁻¹) compared to softer ones (2 mg mL⁻¹). This is evidenced by an increase in the length of the fibers that constitute the cytoskeleton of the cells, as well as a greater number of invading cells and invasion distance. This aligns with previous studies where cells were found to display a compact, rounded shape on softer matrices, whereas on stiffer matrices, they transition to a flattened and extensively spread morphology.^[60] Indeed, this property of the cytoskeleton to dynamically reorganize itself is crucial for GBM progression, and it also varies depending on tumor regions.^[61] In this study, cells in the center of the tumor adopted a more epithelioid morphology, while cells in the invasive front had a more elongated and fibroblast-like shape, with prominent stress fibers.

In addition to promoting tumor aggressiveness, our findings confirm that ECM stiffness acts as a physical barrier to immune cell infiltration and precise delivery of immunotherapeutics,^[62,63] limiting both the distance travelled and the number of infiltrat-

ing immune cells. Tumors with predominance of stiffened regions often exhibit a reduction in immune cell density at their core in comparison to those with lower stiffness. The migration of immune cells within the ECM is governed by the interplay and spatial arrangement of its constituents, with collagen fibers playing a critical role.^[64] A stiffer matrix provides greater resistance, which cells sense and respond to, integrating what is known as mechanotransduction.^[65] In addition, this stiffening may amplify immune evasion by the tumor, altering the expression of TME signaling molecules and decreasing cytotoxic interactions between immune and cancer cells.^[66] Our study of cytokine production revealed that softer matrices enhanced the secretion of pro-inflammatory cytokines, such as IL-12 and TNF- α , whereas stiff matrices promoted immune evasion. TNF- α is largely secreted by M1 macrophages, known to suppress tumor growth. ECM stiffening has been shown to increase colony stimulating factor 1 expression in tumor cells, driving macrophages toward an M2-like state; whereas soft substrates induce the production of reactive oxygen species in macrophages, leading to an M1-like phenotype and resulting in increased secretion of TNF- α .^[67,68] This would explain the reduction in cytokine secretion related to an anti-tumor phenotype in devices with rigid matrices.

TMZ, an oral alkylating chemotherapeutic agent, is the standard treatment for GBM, although 55% of patients are resistant to it.^[69] In our model, TMZ was shown to affect immune cells by reducing both their motility and infiltration into the TME. Although this reduction resolves after 72 h, overall immune cell density remained lower in TMZ-treated devices compared to controls. This is consistent with the lymphopenia induced by TMZ in GBM patients.^[70,71] Interestingly, lymphodepletion induced by TMZ can also have potential benefits.^[72,73] It has been shown to reset the host's immune system, eliminating tolerance to autologous tumor antigens.^[74] Besides, it decreases competition at the surface of antigen-presenting cells, therefore improving cytokine availability, which, in turn, amplifies T-cell activity and depletes Tregs.^[10] These mechanisms are known to improve patient prognosis by enhancing anti-tumor immune response.^[75] Our cytokine analysis supports this hypothesis, showing a temporary boost in anti-tumor cytokine production (IL-12, TNF- α) post-TMZ treatment, although this effect diminishes after 5 days. The latter may result from the exhaustion of T cells due to chronic antigen exposure, leading to reduced effector function related with loss of anti-tumor cytokines.^[76] Aside from a higher anti-tumor response, TMZ does not seem to induce cytotoxicity nor cell death in immune cells, only affecting their speed and motility. These findings lead us to hypothesize about the benefits of using the immune system to our advantage to improve the anti-tumor response in GBM patients, since resistance alone has been shown to be inevitable in most cases. Combining immunotherapy with chemotherapy represents a promising strategy to mitigate the development of resistance to chemotherapy in GBM.

In conclusion, this novel microfluidic device provides a robust platform for modelling complex tumor-immune interaction in GBM. Our findings highlight the critical role of ECM stiffness in regulating immune cell infiltration and tumor cell behavior. We demonstrate that increased matrix stiffness not only impedes immune cell infiltration but also modulates the secretion of key pro-inflammatory cytokines, such as TNF- α and IL-12, emphasizing the intricate crosstalk between the tumor and the immune

system in driving tumor progression. Moreover, the study of TMZ treatment within this model reveals a temporary reduction in immune cell motility, yet underscores its potential to enhance anti-tumor immune responses by reprogramming immune dynamics. The device's ability to faithfully replicate these biological processes offers a valuable tool for advancing our understanding of GBM biology and immune-tumor interactions, providing a platform that could accelerate the development of novel therapeutic strategies and contribute to more effective, personalized treatments.

Supporting Information

Supporting Information is available from the Wiley Online Library or from the author.

Acknowledgements

This work was supported by the Ministry of Science and Innovation, the Agency and the European Regional Development Fund (Project PID2021-126051OB-C41 funded by MCIN /AEI /10.13039/501100011033 / FEDER, UE). This work was supported by the Chips Joint Undertaking (Grant Agreement No. 101140192) and MICIU/AEI/10.13039/501100011033 (PCI2024-153531). This work received funding from the Swiss State Secretariat for Education, Research and Innovation (SERI). Beonchip S.L. would like to acknowledge the financial support received from the Plan de Recuperación, Transformación y Resiliencia. Authors would like to acknowledge the use of Servicio General de Apoyo a la Investigación-SAI, Universidad de Zaragoza and the collaboration of the Plataforma de Apoyo Preclínico (PAP) at the Aragon Health Research Institute (IISA). The authors also thank the patients and the Biobank of the Aragon Health System (PT23/00146) integrated in the Platform ISCIII Biobanks and Biomodels for their collaboration. The authors acknowledge the use of BioRender for generating high-quality scientific illustrations. C.O.R. would like to acknowledge the financial support received from the Spanish Government through a research grant provided by the MINECO fellowship (DIN 2020-011544). C.B. and V.S. would like to thank Gobierno de Aragón (DGA) for the predoctoral funding. The authors thank Gobierno de Aragón and Fondo Social Europeo for the financial help given to TME lab group T62_23R.

Conflict of Interest

I. Ochoa, M. Doblaré, R. Monge and S. Oliván are promoters and consultants for BeOnChip S.L.

Author Contributions

C.B. and C.O.-R. contributed equally to this work. C.B., C.O.R., and V.S. performed conceptualization. C.B., C.O.R., M.A., and V.S. performed methodology and investigation. C.B. and C.O.R. wrote the final manuscript. I.O., R.M., S.O., and V.S. wrote, reviewed, and edited the final manuscript. I.O., M.D., R.M., and S.O. performed resources and funding acquisition. All authors have read and approved the final paper.

Data Availability Statement

The data that support the findings of this study are available in the supplementary material of this article.

Keywords

barrier-free, biomimetic models, extracellular matrix, glioblastoma, immune system, microfluidics, temozolomide, tumor microenvironment

Received: October 8, 2024

Revised: January 17, 2025

Published online: February 3, 2025

- [1] A. Bikfalvi, C. A. da Costa, T. Avril, J.-V. Barnier, L. Bauchet, L. Brisson, P. F. Cartron, H. Castel, E. Chevet, H. Chneiweiss, A. Clavreul, B. Constantin, V. Coronas, T. Daubon, M. Dontenwill, F. Ducray, N. Entz-Werlé, D. Figarella-Branger, I. Fournier, J.-S. Frenel, M. Gabut, T. Galli, J. Gavard, G. Huberfeld, J.-P. Hugnot, A. Idbaih, M.-P. Junier, T. Mathivet, P. Menei, D. Meyronet, et al., *Trends Cancer* **2023**, 9, 9.
- [2] R. Stupp, W. P. Mason, M. J. van den Bent, M. Weller, B. Fisher, M. J. B. Taphoorn, K. Belanger, A. A. Brandes, C. Marosi, U. Bogdahn, J. Curschmann, R. C. Janzer, S. K. Ludwin, T. Gorlia, A. Allgeier, D. Lacombe, J. G. Cairncross, E. Eisenhauer, R. O. Mirimanoff, *N. Engl. J. Med.* **2005**, 352, 987.
- [3] A. Karachi, F. Dastmalchi, D. A. Mitchell, M. Rahman, *Neuro-oncology* **2018**, 12, 1566.
- [4] P. Sharma, A. Aaroe, J. Liang, V. K. Puduvalli, *Neuro-Oncol. Adv.* **2023**, 5, vdad009.
- [5] D. Schiffer, L. Annovazzi, C. Casalone, C. Corona, M. M. Glioblastoma, *Cancers* **2018**, 11, 5.
- [6] D. E. Kuczek, A. M. H. Larsen, M.-L. Thorseth, M. Carretta, A. Kalvisa, M. S. Siersbæk, A. M. C. Simões, A. Roslind, L. H. Engelholm, E. Noessner, M. Donia, I. M. Svane, P. T. Straten, L. Grøntved, D. H. Madsen, *J. Immunother. Cancer* **2019**, 7, 68.
- [7] K. B. Pointer, P. A. Clark, A. B. Schroeder, M. S. Salamat, K. W. Eliceiri, J. S. Kuo, *J. Neurosurg.* **2017**, 126, 1812.
- [8] E. Mohiuddin, H. Wakimoto, *Am. J. Cancer Res.* **2021**, 11, 3742.
- [9] N. Di Ianni, M. Maffezzini, M. Eoli, S. Pellegatta, *Front. Oncol.* **2021**, 11, 747690.
- [10] S. Sengupta, J. Marrinan, C. Frishman, P. Sampath, *Clin Dev. Immunol.* **2012**, 2012, 831090.
- [11] M. C. Kizilarslanoglu, S. Aksoy, N. O. Yildirim, E. Ararat, I. Sahin, K. Altundag, *J BUON Off J Balk Union Oncol.* **2011**, 16, 547.
- [12] X. Niu, Y. Zhang, Y. Wang, *Cancer Pathog Ther* **2023**, 2, 219.
- [13] S. R. Jeong, M. Kang, *Int. J. Mol. Sci.* **2023**, 24, 14609.
- [14] L. Van Os, B. Engelhardt, O. T. Guenat, *Front. Bioeng. Biotechnol.* **2023**, 11, 1191104.
- [15] Y. Chonan, S. Taki, O. Sampetean, H. Saya, R. Sudo, *Integr. Biol.* **2017**, 9, 762.
- [16] C. Bayona, L. Alza, T. Randelovic, M. C. Sallán, A. Visa, C. Cantí, I. Ochoa, S. Oliván, J. Herreros, *Cell Death Dis.* **2024**, 15, 1.
- [17] M. Gerigk, H. Bulstrode, H. H. Shi, F. Tönisen, C. Cerutti, G. Morrison, D. Rowitch, Y. Y. S. Huang, *Lab Chip* **2021**, 21, 2343.
- [18] A. Polini, L. L. del Mercato, A. Barra, Y. S. Zhang, F. Calabi, G. Gigli, *Drug Discov Today* **2019**, 24, 517.
- [19] C. P. Miller, W. Shin, E. H. Ahn, H. J. Kim, D. H. Kim, *Trends Biotechnol.* **2020**, 38, 857.
- [20] Q. Ramadan, R. Hazaymeh, M. Zourob, *Adv. Biol.* **2023**, 7, 2200312.
- [21] L. Businaro, A. De Ninno, G. Schiavoni, V. Lucarini, G. Ciasca, A. Gerardino, F. Belardelli, L. Gabriele, F. Mattei, *Lab Chip* **2012**, 13, 229.
- [22] F. Mattei, G. Schiavoni, A. De Ninno, V. Lucarini, P. Sestili, A. Sistigu, A. Fragale, M. Sanchez, M. Spada, A. Gerardino, F. Belardelli, L. Businaro, L. Gabriele, *J Immunotoxicol* **2014**, 11, 337.
- [23] S. Shim, M. C. Belanger, A. R. Harris, J. M. Munson, R. R. Pompano, *Lab Chip* **2019**, 19, 1013.
- [24] S. Mi, Z. Liu, Z. Du, X. Yi, W. Sun, *Biotechnol. Bioeng.* **2019**, 116, 1731.

- [25] M. Crippa, S. Bersini, M. Gilardi, C. Arrigoni, S. Gamba, A. Falanga, C. Candrian, G. Dubini, M. Vanoni, M. Moretti, *Lab Chip* **2021**, 21, 1061.
- [26] P. S. Nunes, P. D. Ohlsson, O. Ordeig, J. P. Kutter, *Microfluid Nanofluidics* **2010**, 9, 145.
- [27] A. Agha, W. Waheed, N. Alamoodi, B. Mathew, F. Alnaimat, E. Abu-Nada, A. Abderrahmane, A. Alazzam, *Macromol. Mater. Eng.* **2022**, 307, 2200053.
- [28] R. K. Jena, C. Y. Yue, Y. C. Lam, *Microsyst Technol* **2012**, 18, 159.
- [29] C. Olaizola-Rodrigo, S. Palma-Florez, T. Randelovic, C. Bayona, M. Ashrafi, J. Samitier, A. Lagunas, M. Mir, M. Doblaré, I. Ochoa, R. Monge, S. Oliván, *Lab Chip* **2024**, 24, 2094.
- [30] C. Bayona, M. Wrona, T. Randelović, C. Nerín, J. Salafranca, I. Ochoa, *Biofabrication* **2024**, 16, 045002.
- [31] M. Alnæs, J. Blechta, J. Hake, A. Johansson, B. Kehlet, A. Logg, C. Richardson, J. Ring, M. E. Rognes, G. N. Wells, *Arch Numer Softw.* **2015**, 3, 9.
- [32] Z. Chen, J. Zilberberg, W. Lee, *Biomed. Microdevices* **2020**, 22, 58.
- [33] L. J. Kaufman, C. P. Brangwynne, K. E. Kasza, E. Filippidi, V. D. Gordon, T. S. Deisboeck, D. A. Weitz, *Biophys. J.* **2005**, 89, 635.
- [34] B. A. Roeder, K. Kokini, J. E. Sturgis, J. P. Robinson, S. L. Voytik-Harbin, *J. Biomech. Eng.* **2002**, 124, 214.
- [35] S. Motte, L. J. Kaufman, *Biopolymers* **2013**, 99, 35.
- [36] H. Castro-Abril, J. Heras, J. del Barrio, L. Paz, C. Alcaine, M. P. Aliácar, D. Garzón-Alvarado, M. Doblaré, I. Ochoa, *Macromol. Biosci.* **2023**, 23, 2300108.
- [37] S. Parlato, G. Grisanti, G. Sinibaldi, G. Peruzzi, C. M. Casciola, L. Gabriele, *Lab Chip* **2021**, 21, 234.
- [38] J. Galon, D. Bruni, *Immunity* **2020**, 52, 55.
- [39] A. Boussommier-Calleja, R. Li, M. B. Chen, S. C. Wong, R. D. Kamm, *Trends Cancer* **2016**, 2, 6.
- [40] K. Ronaldson-Bouchard, G. Vunjak-Novakovic, *Cell Stem Cell* **2018**, 22, 310.
- [41] M. W. van der Helm, M. Odijk, J.-P. Frimat, A. D. van der Meer, J. C. T. Eijkel, A. van den Berg, L. I. Segerink, *Biosens. Bioelectron.* **2016**, 85, 924.
- [42] O. Mitxelena-Iribarren, C. Olaizola, S. Arana, M. Mujika, *Nanomedicine Nanotechnol Biol Med* **2022**, 39, 102462.
- [43] J. Ahn, M.-J. Yoon, S.-H. Hong, H. Cha, D. Lee, H. S. Koo, J.-E. Ko, J. Lee, S. Oh, N. L. Jeon, Y.-J. Kang, *Hum Reprod Oxf Engl* **2021**, 36, 2720.
- [44] H. Uwamori, T. Higuchi, K. Arai, R. Sudo, *Sci. Rep.* **2017**, 7, 17349.
- [45] C. Soragni, K. Queiroz, C. P. Ng, A. Stok, T. Olivier, D. Tzagkaraki, J. Heijmans, J. Suijker, S. P. M. de Ruiter, A. Olczyk, M. Bokkers, F. Schavemaker, S. J. Trietsch, H. L. Lanz, P. Vulto, J. Joore, *Angiogenesis* **2024**, 27, 37.
- [46] T. Yuan, D. Gao, S. Li, Y. Jiang, *Chin. Chem. Lett.* **2019**, 30, 331.
- [47] J. Loessberg-Zahl, J. Beumer, A. van den Berg, J. C. T. Eijkel, A. D. van der Meer, *Micromachines* **2020**, 11, 1112.
- [48] V. Palacio-Castañeda, L. Kooijman, B. Venzac, W. P. R. Verdurmen, S. Le Gac, *Micromachines* **2020**, 11, 382.
- [49] M. Nikolaev, O. Mitrofanova, N. Broguiere, S. Geraldo, D. Dutta, Y. Tabata, B. Elci, N. Brandenberg, I. Kolotuev, N. Gjorevski, H. Clevers, M. P. Lutolf, *Nature* **2020**, 585, 574.
- [50] N. Gjorevski, M. Nikolaev, T. E. Brown, O. Mitrofanova, N. Brandenberg, F. W. DelRio, F. M. Yavitt, P. Liberali, K. S. Anseth, M. P. Lutolf, *Science* **2022**, 375, eaaw9021.
- [51] G. E. Rainger, C. D. Buckley, D. L. Simmons, G. B. Nash, *Am. J. Physiol.* **1999**, 276, H858.
- [52] G. Radley, S. Ali, I. L. Pieper, C. A. Thornton, *Int. J. Artif. Organs* **2019**, 42, 133.
- [53] E. Roux, P. Bougaran, P. Dufourcq, T. Couffinhal, *Front Physiol* **2020**, 11, 861.
- [54] Y. S. J. Li, J. H. Haga, S. Chien, *J. Biomech.* **2005**, 38, 1949.
- [55] J. Lacombe, F. Zenhausern, *Radiother. Oncol. J. Eur. Soc. Ther. Radiol. Oncol.* **2022**, 176, 187.
- [56] Q. Huang, X. Hu, W. He, Y. Zhao, S. Hao, Q. Wu, S. Li, S. Zhang, M. Shi, *Am. J. Cancer Res.* **2018**, 8, 763.
- [57] L. C. Delon, Z. Guo, A. Oszmiana, C.-C. Chien, R. Gibson, C. Prestidge, B. Thierry, *Biomaterials* **2019**, 225, 119521.
- [58] A. Yui, M. J. Oudin, *Cancer Res.* **2024**, 84, 958.
- [59] Y. A. Miroshnikova, J. K. Mouw, J. M. Barnes, M. W. Pickup, J. N. Lakins, Y. Kim, K. Lobo, A. I. Persson, G. F. Reis, T. R. McKnight, E. C. Holland, J. J. Phillips, V. M. Weaver, *Nat. Cell Biol.* **2016**, 18, 1336.
- [60] J. Schrader, G.-W. TT, R. L. Aucott, M. van Deemter, A. Quaas, S. Walsh, D. Bentes, S. J. Forbes, R. G. Wells, J. P. Iredale, *Hepatology* **2011**, 53, 1192.
- [61] M. Keller, M. Blom, L. L. Conze, M. Guo, D. Hägerstrand, P. Aspenström, *Sci. Rep.* **2022**, 12, 9838.
- [62] Z. Mai, Y. Lin, P. Lin, X. Zhao, L. Cui, *Cell Death Dis.* **2024**, 15, 1.
- [63] C. W. Yoon, Y. Pan, Y. Wang, *Front Cell Dev Biol* **2022**, 10, 1064484.
- [64] R. Hallmann, X. Zhang, J. Di Russo, L. Li, J. Song, M.-J. Hannocks, L. Sorokin, *Curr. Opin. Cell Biol.* **2015**, 36, 54.
- [65] A. Saraswathibhatla, D. Indana, O. Chaudhuri, *Nat. Rev. Mol. Cell Biol.* **2023**, 24, 495.
- [66] E. Peranzoni, A. Rivas-Cacedo, H. Bougherara, H. Salmon, E. Donnadieu, *Cell Mol. Life Sci. CMLS* **2013**, 70, 4431.
- [67] Y. C. Chuang, H. M. Chang, C. Y. Li, Y. Cui, C. L. Lee, C. S. Chen, *ACS Appl. Mater. Interfaces* **2020**, 12, 48432.
- [68] M. Chen, Y. Zhang, P. Zhou, X. Liu, H. Zhao, X. Zhou, Q. Shi, *Bioact. Mater.* **2020**, 5, 880.
- [69] M. M. Mrugala, M. C. Chamberlain, *Nat. Clin. Pract. Oncol.* **2008**, 5, 476.
- [70] A. J. Lin, J. L. Campian, C. Hui, S. Rudra, Y. J. Rao, D. Thotala, D. Hallahan, J. Huang, *J. Neurooncol.* **2018**, 136, 403.
- [71] S. A. Grossman, X. Ye, G. Lesser, A. Sloan, H. Carraway, S. Desideri, S. Piantadosi, *Clin Cancer Res Off J Am Assoc Cancer Res* **2011**, 17, 5473.
- [72] J. H. Sampson, K. D. Aldape, G. E. Archer, A. Coan, A. Desjardins, A. H. Friedman, H. S. Friedman, M. R. Gilbert, J. E. Herndon, R. E. McLendon, D. A. Mitchell, D. A. Reardon, R. Sawaya, R. Schmittling, W. Shi, J. J. Vredenburgh, D. D. Bigner, A. B. Heimberger, *Neuro-Oncol* **2011**, 13, 324.
- [73] K. A. Batich, E. A. Reap, G. E. Archer, L. Sanchez-Perez, S. K. Nair, R. J. Schmittling, P. Norberg, W. Xie, J. E. Herndon, P. Healy, R. E. McLendon, A. H. Friedman, H. S. Friedman, D. Bigner, G. Vlahovic, D. A. Mitchell, J. H. Sampson, *Clin. Cancer Res. Off J. Am. Assoc. Cancer Res.* **2017**, 23, 1898.
- [74] K. W. Tan, M. Evrard, M. Tham, M. Hong, C. Huang, M. Kato, A. Prevost-Blondel, E. Donnadieu, L. G. Ng, J.-P. Abastado, *Oncoimmunology* **2015**, 4, 978709.
- [75] N. F. Brown, T. J. Carter, D. Ottaviani, P. Mulholland, *Br. J. Cancer* **2018**, 119, 1171.
- [76] E. Jenkins, T. Whitehead, M. Fellermeier, S. J. Davis, S. Sharma, *Oxf. Open Immunol.* **2023**, 4, iqad006.